Towards a Universal Veering Profile for Turbulent Ekman Flow at arbitrary Reynolds number - Part 2

LES and DNS of Turbulent Ekman Flow

Hauke Wurps and Cedrick Ansorge

Draft June 28, 2024

Abstract

Turbulent Ekman flow is a canonical flow representation of the atmospheric boundary layer, characterized by a logarithmic increase of the wind speed near the surface and a turning of the wind vector aloft. In part I of this work, we derived a formulation of the mean wind velocity profiles of the stationary turbulent Ekman flow based on direct numerical simulation (DNS). Here, we explore the extrapolation of these profiles to atmospheric Reynolds numbers using large-eddy simulation (LES). We compare theoretical profiles of the wind vector for low Reynolds-number turbulent Ekman flow to results from DNS and LES. This necessitates the inclusion of viscous effects, usually neglected in LES, along with modifications to the standard bottom boundary condition. Analysis of the grid-convergence for higher resolution unveils a convergence of LES data towards the theoretical profiles for both intermediate and high Reynolds numbers. Our LES thus confirm that–within the logarithmic layer (the lowest 10 % of the boundary layer)— the turning of the wind vector rotates by approximately one-third of its total rotation across the entirety of the boundary layer. Such agreement of our theoretical formulation and LES data raises our confidence in the underlying assumptions of the theory and thus reinforces the utility of the theoretical profiles as a reference for intermediate and a quasi-reference for higher Reynolds number simulations.

Keywords— Large-Eddy Simulation · Scale separation · Ekman layer · Prandtl layer · Hodograph

1 Introduction

The interaction of atmospheric boundary layer (ABL) flow with its lower boundary condition, the surface, is a defining property of the ABL [Stull, 1988]. Relevant aspects of the interaction with the boundary not only include its heterogeneity [Avissar and Pielke, 1989, Giorgi and Avissar, 1997, Claussen, 1991, Garratt, 1990] and roughness [Monin, 1970, Brutsaert, 1975, Raupach et al., 1991, Kostelecky and Ansorge, 2024], but also a wind veer in favor of the pressure gradient force when the surface is approaced [Ekman, 1905]. An important tool with capabilities to model the flow-surface interaction is Large-Eddy Simulation (LES). Indeed, LES is widely used to model turbulent flow in the atmospheric boundary layer (ABL) [Stoll et al., 2020]. This includes various applications, such as simulating wind turbine and wind farm wakes, and interactions within wind farm clusters [Porté-Agel et al., 2011, Mehta et al., 2014, Breton et al., 2017]. Furthermore, LES is applied in complex environments like mountainous or urban areas [Stoll et al., 2020, García-Sánchez et al., 2018] and to investigate the dispersion of pollution Han et al. [2018]. These applications typically focus on the lower segment of the ABL on the rotating earth, known as the Prandtl or surface layer. In this layer, the vertical wind speed profile commonly exhibits a logarithmic increase, followed by a prominent change of wind direction within the Ekman layer above. Accurate characterization of how wind speed and direction vary with height is of great importance for wind-power forecasting and projection [Optis et al., 2014].

The simplest representation of the ABL taking into account rotation *and* the quasi non-turbulent, free atmosphere aloft is the turbulent Ekman flow. It is a horizontally homogeneous,

statistically stationary boundary-layer flow over a rotating flat surface. Here we consider the problem under neutral stratification, where the potential temperature is constant across the whole domain. Turbulent Ekman flow shows the key characteristics shaping the real ABL: a logarithmic layer and the Ekman spiral. Near the surface, viscous forces dominate the flow. The stationary ABL-height is then defined by the interplay between turbulent growth due to the shear instability of the configuration [Lilly, 1966] and rotational suppression of turbulence due to the Coriolis effect. The system's statistical equilibrium is defined by one single parameter, the Reynolds number **Re**, signifying the scale separation between the largest and smallest scale within the problem. The largest scales are given by shear-induced eddies constrained by the boundary layer's height, while the smallest scales reside within the dissipative range, where strong viscous forces suppress turbulence. The dimensional mean solution of the turbulent Ekman layer is influenced by three parameters: the geostrophic wind G, the Coriolis parameter f, and the kinematic viscosity ν. These three parameters define the Reynolds number $Re_D = GD/\nu$. With $D = \sqrt{2\nu/f}$ the Ekman layer depth of a laminar flow we write

$$Re_D = \sqrt{2}\frac{G}{\sqrt{\nu f}} \tag{1}$$

The mean solutions of the velocity components are functions of only the Reynolds number and the height above the ground z: $u(\mathbf{Re}_D, z)$, $v(\mathbf{Re}_D, z)$ (see e.g. Csanady [1967]).

Part I of this publication, presents a framework to predict wind direction and speed across the turbulent Ekman flow, drawing from the works of Csanady [1967], Tennekes [1973], and Spalart [1989]. As Spalart [1989], we use G, f, and ν to derive the friction velocity $u_\star$ and the angle $\alpha_\star$ between geostrophic wind and shear stress at the wall. While earlier descriptions of the turbulent Ekman layer were limited to specific parts of the boundary layer, we derive mean velocity profiles covering the entire ABL with due regard of changes in the Reynolds number. We have shown that the theoretical velocity profiles are in excellent agreement with DNS for intermediate Reynolds numbers.

However, it remains uncertain, if the extrapolation of the above framework towards atmospheric **Re** is valid. The substantial separation of scales in the ABL renders direct numerical simulation (DNS) of the entire turbulent flow at scale impossible. Within the framework of LES, only the larger eddies are resolved, that contain the main share of kinetic energy, while turbulent mixing below the subfilter-scale is parameterized. This technique allows for the simulation of the ABL at very high (atmospheric) **Re**.

The accurate representation of mean profiles of velocity, i.e. of first-order statistics of the wind field, is commonly assumed when using LES in a predictive manner [Fedorovich et al., 2004]. Here, we compare LES outcomes to theoretical solutions to determine the validity of this assumption under different conditions. As LES introduces the grid size as an additional parameter (often understood in relation to a filter scale, cf. Pope [2004]), we conduct a thorough analysis of its impact on simulation results. Esau [2004] and Jiang et al. [2018] have executed similar LES analyses of neutral Ekman layers, however, they introduce an additional parameter by selecting an arbitrary roughness length z_0, whereas we derive the parameter z_0 corresponding to a fluid with a kinematic viscosity of $\nu = 1.5 \cdot 10^{-5}$ over flat surface.

Here, we examine three different Reynolds numbers Re_D: 1600, $1.5 \cdot 10^5$, and 10^6. While the case $Re_D = 1600$ is also investigated by DNS (cf. part 1 of this study), $Re_D = 1.5 \cdot 10^5$ and 10^6 correspond to the scale separation found in typical atmospheric boundary layers. For $Re_D = 1600$, we compare DNS and LES results using the exact same forcing and settings. This is the first comparison of this kind for the turbulent Ekman flow. The LES results converge to the DNS results with decreasing grid cell size. This approach raises our confidence in the LES results to a new level for the direct comparison with a resolving simulation. Furthermore, it allows us to extend the insight from DNS to atmospheric scale where an approach through DNS

is clearly infeasible for computational constraints. We observe a clear **Re** dependency in the LES results, matching the predictions of the theoretical framework.

The content is structured as follows. Section 2 provides a complete mathematical description of the turbulent Ekman layer's velocity profiles. A description of the simulated cases and the numerical set-up is given in section 3, followed by the presentation of results and its comparison to the theoretical profiles in section 4. We conclude in section 5.

2 A Universal Velocity Profile for the Turbulent Ekman Layer

In this chapter, we introduce the velocity profile for the turbulent Ekman layer developed in part I. We align the coordinate Ox with the surface stress, Oz points normal to the surface and normal to Ox, and Oy in the span-wise direction, normal to Oxz. In proximity to the lower boundary, the boundary layer scales in viscous (inner) units, denoted by the index "+" ($z^+ = zu_\star/\nu$, $U^+ = U/u_\star$, where U is the velocity component in x-direction and $u_\star = \sqrt{\nu\partial_z U}$ the friction velocity). From the top perspective, the profiles converge when scaled using outer units, denoted by the index "−" ($z^- = z/\delta$, $U^- = U/G$, where $\delta = u_\star/f$ is the boundary-layer depth scale, f the Coriolis parameter and G the geostrophic wind speed). At the lower boundary, the x-axis of the inner units aligns with the shear stress, while the x-axis of the outer units aligns with the geostrophic wind. The angle between both axes is denoted as $\alpha_\star$, the surface veer of the wind across the boundary layer. Profiles of the velocity components are studied in three different layers reflecting the change of dominant balance when moving away from the surface. These are (i) the Ekman layer denoted $(\cdot)_{\mathrm{Ek}}$ (Sec. 2.1), (ii) the viscous sub-layer, denoted by an index $(\cdot)_{\mathrm{visc}}$, and (iii) the logarithmic layer denoted by $(\cdot)_{\log}$ We match U_{visc} and $U_{\log}$ according to their respective formulations and combine them to U_{inner} (Sec. 2.2). Inner and outer profiles are then matched by a weighting transfer function based on the error function.

The geostrophic drag, i.e. normalized friction $Z \equiv u_\star/G$, and $\alpha_\star$ form the basis of the boundary-layer scaling, and they are estimated using the semi-empirical drag-law introduced by Spalart [1989], which describes them as functions of only the Reynolds number:

$$\frac{G}{u_\star}\cos\phi^\star = \frac{1}{\kappa}\log Re_\tau + C - A_r, \tag{2a}$$

$$\sin\phi^\star = A_i\frac{u_\star}{G}, \tag{2b}$$

$$\alpha_\star = \phi^\star - \frac{C_5}{Re_\tau}, \tag{2c}$$

$$Re_\tau = \frac{u_\star^2}{\nu f}\left(= \frac{1}{2}Re_D^2\frac{u_\star^2}{G^2}\right), \tag{2d}$$

where we use $\kappa = 0.416$, $A_r = 4.80$, $A_i = -5.57$, $C = 5.4605$, $C_5 = -57.8$ based on the DNS data available (cf. Part I, Ansorge and Mellado [2014]).

2.1 Ekman layer

The outer layer of the ABL is characterized by a triadic balance between turbulent flux, pressure gradient and the Coriolis; the vertical change of the Coriolis force causes a pronounced height dependence of the wind direction resulting in the Ekman spiral [Ekman, 1905]. The classic solution employs Ekman dynamics down to the surface—and thus also in the surface layer, where this is a rather poor representation of turbulent mixing. Here, we model the surface layer by a lower boundary condition for the Ekman spiral determined from DNS:

$$U_{EK} = G + Ae^{-\tilde{z}}\cos\tilde{z}, \tag{3a}$$

$$V_{EK} = -Ae^{-\tilde{z}}\sin\tilde{z}, \tag{3b}$$

where the x-axis is aligned with the geostrophic wind and $A = 8.4u_\star$, $\tilde{z} = (z - z_r)/D_E$, $z_r = 0.12\delta$, and $D_E = 3\delta/4\pi \approx 0.24\delta$. The transition from the logarithmic layer to the Ekman layer is located at $z^- = 0.28 - 2.25Re_D^{-1/2}$ with a transition scale of $\sigma_T = 2$ for the stream-wise velocity.

2.2 Inner and viscous layers

In the viscous sublayer, the shear-aligned velocity $U^{\alpha_\star}$ is described by the law of the wall $U^{\alpha_\star +} = z^+$ and the span-wise velocity $V^{\alpha_\star}$ is zero by choice of the reference frame (the index $\alpha_\star$ indicates the alignment with the direction of the shear stress). Around $z^+ = 5$, the velocity begins to deviate from linearity, and the buffer layer forms the transition from the viscous to the logarithmic layer. From the surface up to the buffer layer, the stream-wise velocity is described by

$$U^{\alpha_\star +}_{\text{buffer}} = \frac{z^+}{1 + c_1(z^+)^2} + (c_2 z^+ - a_{\text{match}}) \frac{1 + \tanh[0.2(z^+ - 22)]}{2} + c_3 e^{-c_4(z^+ - 22)^2}. \tag{4a}$$

With $c_1 = 0.00185$, $c_2 = 0.195$, $c_3 = 0.4$, $c_4 = 0.35$. The coefficient $a_{match} = 3.5727$ is chosen to match the u-profile in the logarithmic layer above at $z^+ = 40$, such that

$$U^{\alpha_\star +}_{\text{inner}} = \begin{cases} U^{\alpha_\star +}_{\text{buffer}}, & z^+ \leq 40. \\ \kappa^{-1} \log z^+ + C & z^+ > 40. \end{cases} \tag{4b}$$

with the von-Kármán constant $\kappa = 0.416$, and $C = 5.4605$ as in the estimation of the geostrophic drag in Eq. (2).

For the span-wise velocity, the boundary conditions and Ekman dynamics imply that

$$V^{\alpha_\star}_{\text{visc}} \delta^+ \sim G f_V(z^+), \tag{5a}$$

where f_V is a universal, non-dimensional function (cf. Part I). Above the viscous layer, scaling arguments are scarce, but there is evidence for a logarithmic scaling of also the span-wise velocity component. We hence use

$$V^{\alpha_\star}_{\text{inner}} = \begin{cases} V^{\alpha_\star}_{\text{visc}} &= \dfrac{G}{\delta^+} v_{ref}(w_v z^+ - 1 + exp[-w_v z^+]) \quad z^+ \leq 10 \\ V^{\alpha_\star}_{\text{log}} &= \dfrac{G}{\delta^+}(a_{log} + b_{log} \log(z^+) + c_{log} z^+) \quad z^+ > 10. \end{cases} \tag{5b}$$

with $v_{\text{ref}} = 18.85$ and $w_v = 0.2353$ leads to excellent agreement with the DNS data. The coefficients $a_{\log}, b_{\log}$, and $c_{\log}$ are determined by (i)-(ii) a smooth transition to V_{visc} at $z^+ = 10$, and (iii) the condition $V_{\log}(z^- = 0.3) = V_{\text{EK}}(z^- = 0.3) =: v_{03}$ (cf. Part I). For the Reynolds-number dependency of the Ekman-layer profiles, $V_{\text{Ek}}(z^- = 0.3)$ depends on Re, such that the coefficients exhibit a weak dependence on Re.

2.3 Transition from inner to outer profiles, synopsis

A smooth transition between consecutive layers is achieved using a transfer function:

$$w_* = \frac{1}{2}\left(\text{erf}\left[\sigma_T \log\left(\frac{z}{z_T}\right)\right] + 1\right), \tag{6}$$

where erf is the error function, σ_T is a transition scale that defines the width of the transition and z_T is the height of the transition, where the upper and the lower layer equally contribute to the velocity ($w_*(z_T) = 0.5$). The inner profiles U_{inner} and V_{inner} are blended to the Ekman profile using eq. (7) with $\sigma_T = 2$ and $z_T^- = 0.28 - 2.25\sqrt{1/Re_D}$.

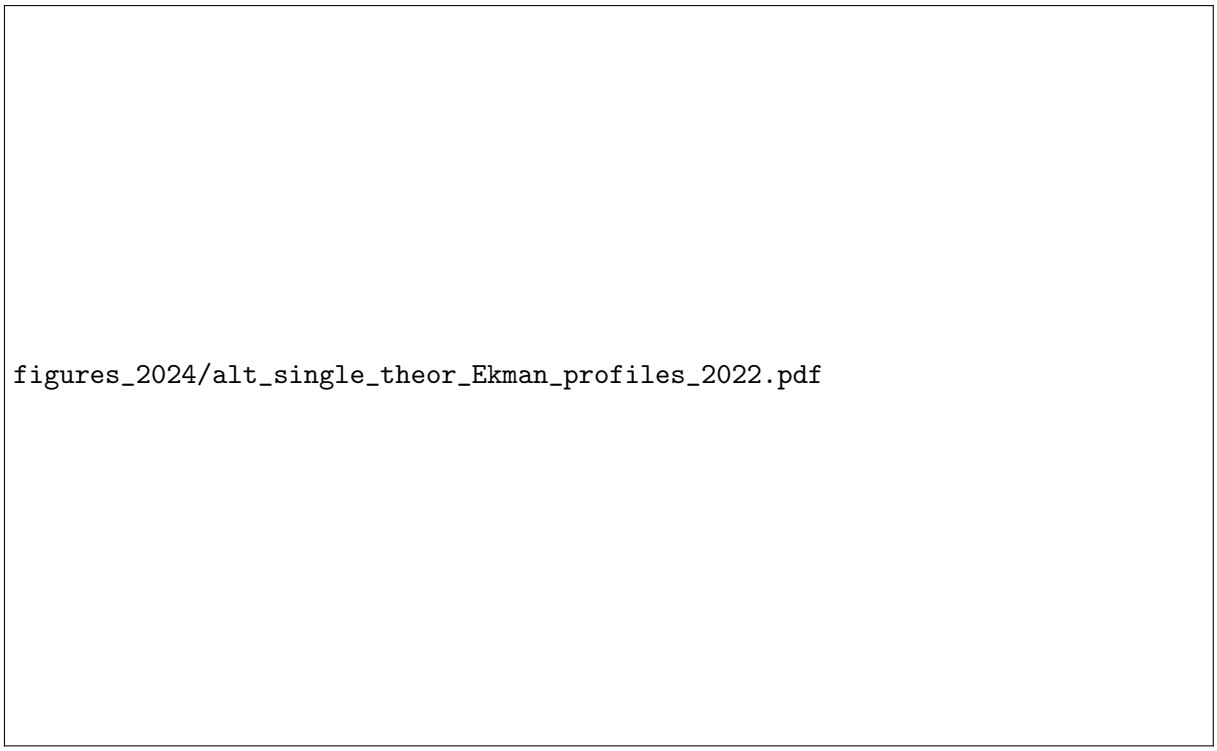

Figure 1: a) Theoretical shear-aligned velocity profile (U^+,$-V^+$) of the turbulent Ekman flow for $Re_D = 2000$ (——) and $Re_D = 4000$ (- - - -) and the different layers (colors). b) Hodograph of the geostrophy-aligned velocity components

.

$$U = (1 - w_{outer})U_{inner} + w_{outer}U_{EK}, \tag{7a}$$

$$V = (1 - w_{outer})V_{inner} + w_{outer}V_{EK}. \tag{7b}$$

The velocity profiles are given for two Reynolds numbers in Fig. 1. In the viscous sublayer, the shear-aligned component U^+ increases linearly with height up $z^+ \approx 5$. In between $5 \lesssim z^+ \lesssim 30$, we find the buffer layer with a transition from the linear law-of-the-wall to the logarithmic law. Above $z^+ \approx 30$, the logarithmic layer begins. Then, U^+ increases logarithmically up to the Ekman layer and reaches its supergeostrophic maximum. Above, it decreases to its free-stream geostrophic value. The depth of the logarithmic layer increases with **Re**. The spanwise component V^+ remains close to zero up to the middle of the logarithmic layer, where the transition to the Ekman layer takes place ($z^- \approx 0.28 - 2.25\sqrt{1/Re_D}$). The profiles of V^+ of all Reynolds numbers have a similar shape but are shifted in z^+. The similar V^+ and the growth of U^+ leads to a smaller angle $\alpha_\star$ between surface shear stress and geostrophic wind for higher **Re**, which is visible in the hodograph.

3 Case description and numerical set-up

3.1 Settings

An incompressible, turbulent Ekman flow over a hydrodynamically smooth surface is simulated using the Parallel Large Eddy Simulation model (PALM, Maronga et al., 2020a). We study three different Reynolds numbers $\mathrm{Re}_D = 10^3; 1.5 \times 10^5; 10^6$, hereafter Re1, Re2, and Re3, respectively (Tab. 1). The domain is rotating around the z-axis with an angular velocity corresponding to the Coriolis parameter $f = 10^{-4}s^{-1}$. The stratification of the flow is truly neutral, i.e., the potential

Table 1: Parameters of the simulated cases. f, ν, and G are input parameters and define the Reynolds numbers Re_D and Re_τ, while $u_\star$, $\alpha_\star$, and $\delta = u_\star/f$ are resulting properties of the flow

Name	Re_D	Re_τ	f [s^{-1}]	ν [$\mathrm{m}^2\mathrm{s}^{-1}$]	G [ms^{-1}]	$u_\star$ [ms^{-1}]	$\alpha_\star$ [°]	δ [m]
Re1	1.6×10^3	3.0×10^3			0.0438	0.00211	16.8	21.1
Re2	1.5×10^5	7.3×10^6	10^{-4}	1.5×10^{-5}	4.108	0.1048	8.5	1048
Re3	1×10^6	2.2×10^8			27.39	0.5785	7.0	5785

Table 2: Simulations and grid parameters: ReX stands for one of the Reynolds numbers Re1, Re2, and Re3. Δ is the grid cell size, $\delta = u_\star/f$ is the boundary layer height, n_i is the number of grid cells in the direction O_i, L_x and L_z are the domain sizes in the horizontal and vertical direction, respectively

Name	Δ^-	n_x	n_y	n_z	L_x/δ	L_z/δ
ReX_50	1/50	144	144	128	2.88	5.0
ReX_100	1/100	288	288	216	2.88	4.5
ReX_150	1/150	432	432	288	2.88	3.7
ReX_200	1/200	576	576	384	2.88	4.1
ReX_dyn	1/200	576	576	384	2.88	4.1

temperature is constant across the whole domain. A constant boundary layer height on the order of $\delta = u_\star/f$ forms due to the balance between shear production and rotational suppression of turbulence. At the upper boundary, the flow is non-turbulent. Hence, a no-penetration boundary condition is used for the vertical velocity component while the horizontal components are prescribed according to geostrophic balance–a Dirichlet-type boundary condition. At the bottom, a constant-flux layer is assumed and Monin–Obukhov similarity theory (MOST) is used to calculate the surface momentum fluxes. The Navier-Stokes equations are integrated using a 3^{rd}-order low-storage Runge–Kutta method. For scalar advection a 5^{th}-order Wicker–Skamarock scheme is employed. The Poisson equation is solved using a direct fast Fourier transform (FFT). In LES, the turbulent transport on the subgrid scale (SGS) needs to be modeled by an SGS closure model. We use two kinds of SGS closures to assess their impact on the LES solution: a 1.5-order closure after Deardorff [1980] and a dynamic closure after Heinz [2008]. For most of the simulations, the 1.5-order closure is used, since the dynamic closure needs more computational resources, but the simulations with $\Delta^- = 200^{-1}$ are repeated using the dynamic closure.

To study the effect of resolution on the simulations, four different grid resolutions are chosen for each Reynolds number case. The grid cell size Δ is around $\delta/50$, $\delta/100$, $\delta/150$, and $\delta/200$, one coarse, two medium, and one fine resolution, respectively (see table 2). In total, 15 simulations are carried out. The grid spacing inside the boundary layer is isotropic up to $z = 1.3\delta$. Aloft, the grid spacing along Oz is stretched by 3% per grid point until a maximum spacing of $(\Delta z)_{\max} = 6\Delta x$ is reached. The number of vertical grid points is chosen such that $L_z \geq 3\delta$. Different domain heights are caused by numerical requirements of the FFT-solver. In the upper third of the domain, Rayleigh damping is active to avoid wave reflections from the top boundary.

The flow is initialized with wind speed profiles based on a one-dimensional model with a Reynolds-average based turbulence parametrization. At the beginning of the simulation, random perturbations are imposed on the velocity field to trigger turbulence. The resulting imbalance between pressure force and Coriolis force results in an inertial oscillation of the period $T_{io} = 2\pi/f$, where a part of the flow's mean kinetic energy oscillates between U- and V-component. The oscillation decays over time and would eventually vanish for large time. In order to obtain profiles in statistical equilibrium of the flow, we use a spin-up time of 1.5 T_{io} and perform a horizontal domain average over 2 T_{io}.

In part I of this publication, the DNS of $Re_D \leq 1\,600$ is carried out for a horizontal domain size of $(0.54\Lambda_{Ro})^2$ - $(1.08\Lambda_{Ro})^2$, where $\Lambda_{Ro} = G/f$ is the Rossby radius. For these Reynolds numbers, $Z \approx 0.05$, such that $L_x \approx 10\delta$. However, Z decreases logarithmically with increasing Reynolds number and it is $Z \approx 0.02$ for $Re_D = 10^6$. A domain size of half the Rossby radius would then extend to $L_x \approx 25\delta$. Such a large domain would imply immense computational cost. Spalart et al. [2008] used a horizontal domain of $L_x = 2\delta$, arguing that this length allows the resolution of the largest outer-layer eddies according to Csanady [1967]. During a sensitivity test of the domain size we observed that simulations with domain sizes $L \geq 4\delta$ often tend to accumulate turbulence kinetic energy in the upper half of the the boundary layer. This TKE increases over several inertial oscillations with energy mostly on the scale of the domain size. Such a development was not observed in the DNS. We could successfully avoid such a behaviour by using a domain of size $L \approx 3\delta$ in combination with a shifted periodic boundary condition in y-direction, as described by Munters et al. [2016]. Although for the Ekman flow the direction of the mean flow is only aligned with the x-direction of the grid near the surface, a shift of the boundary condition by $L/3$ significantly helped to suppress the accumulation of TKE in the upper half of the boundary layer.

3.2 Viscosity and roughness length

In LES, one postulates that a sufficient part of the largest eddies is resolved so as to represent the dominant non-linear effects of turbulent mixing [Pope, 2004]. Below these resolved scales, turbulence is modeled as a more or less isotropically acting diffusive agent by a closure model (dynamic, Deardorff, see above). Thus, molecular friction is not considered directly, but only by virtue of a turbulence model linking the resolved and dissipative scales. In their seminal works on the spectral energy transfer in homogeneous isotropic turbulence, Kolmogorov [1941] and Obukhov [1941] showed that the energy transfer rate across the spectrum is in fact constant provided that both dissipation and production terms can be neglected. This implies that the transfer rate across the cut-off scale in LES does not depend on the magnitude of the viscous scale, presupposed that (i) the cut-off scale of the LES is well within the inertial range and (ii) the LES turbulence is approximately isotropic and homogeneous at the smallest resolved scales. Consequently, SGS-models of LES do not necessarily require explicit information about the actual viscosity of the fluid or other viscous parameters.

In LES at low **Re** or very high resolution the subgrid eddy viscosities may fall far below the molecular viscosity of air. In the context of PALM's Deardorff closure, it is $K_m = c_0\Delta\sqrt{e}$, where $c_0 = 0.1$ [Deardorff, 1980], Δ is the grid size and e is the SGS-TKE, calculated by a prognostic equation. Hence, very low e as well as fine resolution can lead to $K_m < \nu$. When this is the case, ν cannot be ignored anymore, and we let $K_m = c_0\Delta\sqrt{e} + \nu$. Hence, (absent stratification) the governing equation of for momentum in our version of PALM is

$$\frac{\partial u_i}{\partial t} = -\frac{\partial u_i u_j}{\partial x_j} - \epsilon_{ijk} f_j u_k + \epsilon_{i3j} f_3 u_{g,j} - \frac{1}{\rho_0}\frac{\partial \pi^*}{\partial x_i} + \frac{\partial}{\partial x_j}\left(K_m\left(\frac{\partial u_i}{\partial x_j} + \frac{\partial u_j}{\partial x_i}\right)\right). \tag{8}$$

In the limit of either well-resolved simulations or low **Re** (or both), $K_m \to \nu$, so the last term on the right hand side of eq. (8) becomes $\nu\frac{\partial^2 u_i}{\partial x_j^2}$, which complies with the Navier-Stokes equations for an incompressible fluid underlying our reference solution from DNS.

In contrast to the interior closure of the LES where the direct effect of ν is of small relevance compared to the eddy viscosity—at least for high **Re**—, this is not true for the viscid effects at the bottom boundary: A constant flux layer is assumed in between the first grid point and the lowermost half point (on the Arakawa-C staggered grid) to estimate friction velocity and surface

stresses by MOST:

$$u_\star = \frac{\kappa(U^2+V^2)^{0.5}}{\ln\left(z/z_0\right)}, \tag{9}$$

$$-\overline{u''w''}_0 = \frac{\kappa U u_\star}{\ln\left(z/z_0\right)}, \tag{10}$$

where double dashes refer to the unresolved, i.e. SGS-parameterized, fluctuations. In these expressions, viscosity enters indirectly by virtue of the roughness length z_0 when considering the law of the wall for a smooth surface:

$$u^+ = \frac{1}{\kappa}\ln(z^+) + C^+ = \frac{1}{\kappa}\ln\left(\frac{z^+}{z_0^+}\right). \tag{11}$$

For aerodynamically smooth flow, it is $z_0^+ = 0.1031$ based on Eq. 4b. (This is known to be the minimal roughness length of a turbulent boundary layer; see e.g. Kraus, 2008.) Hence,

$$z_0 = z_0^+ \frac{\nu}{u_\star} \approx 0.1\frac{\nu}{u_\star} \tag{12}$$

depends on the viscosity ν of the fluid. In other words, given fixed surface properties, a choice for z_0 implies a particular value for the viscosity ν.

When using MOST for the surface fluxes it is assumed that the height of the first grid point lies inside of the logarithmic layer. Again, the limit of low **Re** and high resolution requires adaptations to this boundary condition. In the case of very fine resolution, the first grid point might fall into the buffer layer or even the viscous layer of the flow, so the equations of MOST are no longer adequate to calculate the local stress. To avoid that, we follow the recommendation of Kawai and Larsson [2012] and use the horizontal velocity from a higher layer z_{sl} to compute the mean stress in the constant flux layer. Further, we adopt the boundary condition suggested by Maronga et al. [2020b] and use domain averaged velocities for the estimation $u_\star$:

$$u_\star \approx u_{*,mean} = \frac{\kappa < u_h(z_{sl}) >}{\ln(z_{sl}/z_0)}, \tag{13}$$

where $u_h = \sqrt{u^2+v^2}$ and angle brackets refer to the horizontal average over the entire domain. The mean stress is then used as a boundary condition at the first grid point ($z = z_1$). It is distributed locally to the unresolved stresses in x- and y-direction via

$$\overline{u''w''}_0(x,y,z_1) = -u_{*,mean}^2 \frac{u(x,y,z_1)}{\sqrt{< u >^2 (z_1) + < v >^2 (z_1)}}, \tag{14}$$

and accordingly for $\overline{v''w''}_0$. This way, the domain average of the stress components yield the total stress of eq. 13 ($u_{*,mean}^2 = \sqrt{< \overline{u''w''}_0 >^2 + < \overline{v''w''}_0 >^2}$). For the reference height we use the grid level closest to $z_{sl}^- \approx 0.1$. This alleviates two problems: First, z_{sl} is within log-layer. Second, the flow at $z = z_{sl}$ is better resolved than closer to the surface.

4 Results and Discussion

In this chapter, we compare the results from the LES to the theoretical bulk parameters (4.1) and velocity profiles (4.2) and discuss the dynamics of the turbulent flow in LES.

Table 3: LES results: Δ^+ is the grid cell size in wall units, $u_\star$ the friction velocty, $\alpha_\star$ the angle between geostrophic wind and negative surface shear stress, κ_{LES} the Kármán-measure of the logarithmic layer (estimated by linear regression), C^+ the intercept (see eq. 4b), and δ_{95} the height estimated by a linear interpolation of the shear stress reduction to 95% of its surface value

Name	Δ^+	$u_\star/u_{\star,th}$	$\alpha_{\star,th}-\alpha_\star$	κ_{LES}	C^+	δ_{95}/δ
Re1_50	59	1.021	1.5°	-	-	0.71
Re1_100	30	1.008	1.1°	0.52	8.3	0.66
Re1_150	20	1.004	1.0°	0.48	7.0	0.64
Re1_200	15	1.003	0.7°	0.46	6.5	0.62
Re1_dyn	15	1.002	0.9°	0.43	5.7	0.58
Re2_50	1.5×10^5	1.008	1.1°	-	-	0.77
Re2_100	7.3×10^4	1.001	0.5°	0.53	12.2	0.66
Re2_150	4.9×10^4	1.000	0.2°	0.47	8.9	0.60
Re2_200	3.7×10^4	1.000	0.1°	0.44	6.8	0.59
Re2_dyn	3.7×10^4	1.000	0.0°	0.42	5.6	0.55
Re3_50	4.5×10^6	1.007	0.7°	-	-	0.76
Re3_100	2.2×10^6	1.001	0.5°	0.53	14.3	0.65
Re3_150	1.5×10^6	1.000	0.3°	0.47	10.3	0.60
Re3_200	1.1×10^6	1.001	0.1°	0.44	7.7	0.59
Re3_dyn	1.1×10^6	1.000	0.2°	0.43	6.7	0.56

4.1 Bulk parameters

The geostrophic drag $Z = u_\star/G$ quantifies the conversion of mean-flow kinetic energy (G^2) to turbulence ($u_\star^2$). The ratio of $u_\star$ resulting from the simulations to the theoretical value $u_{\star,th}$ are shown in Tab. 3. All values are close to one, while the strongest deviations are observed for the simulations with the coarsest resolutions. A slight dependence on the resolution can be observed for Re1, as $u_\star$ steadily approaches $u_{\star,th}$ with increasing resolution. For Re2 and Re3, all but the coarsest resolution nearly exactly match the theoretical value. The choice of z_0 and the geostrophic wind G determine the magnitude of $u_\star$ in a non-trivial way. From a top perspective, the horizontal velocity increases from its geostrophic value to the supergeostrophic maximum and then decreases with decreasing height. The horizontal mean velocity at the grid point closest to $z^- = 0.1$ is used to calculate $u_\star$ according to Eq. (13). It is remarkable that the choice of $z_0^+ = 0.1031$ leads to a value of $u_\star$ very close to the prediction by semi-empirical considerations (cf. Spalart [1989]).

The surface veering $\alpha_\star$ is key to quantify the Ekman pumping and of central relevance for larger-scale applications. For the LES, we use the first derivatives of the velocity components calculated by 3$^{\text{rd}}$-order forward finite differences to estimate $\alpha_\star$:

$$\alpha_\star = \arctan\left(\left\langle\frac{\partial v}{\partial z}\right\rangle_0 \Big/ \left\langle\frac{\partial u}{\partial z}\right\rangle_0\right) - \arctan\left(\frac{V_G}{U_G}\right). \tag{15}$$

Table 3 shows that nearly all LES yield an $\alpha_\star$ smaller than the theoretical value $\alpha_{\star,\text{th}}$. In general, we observe an increase of $\alpha_\star$ with resolution. The finest resolution of Re2 and Re3 generally align closely with the theoretical direction while for Re1_200 still 0.9° is missing. Fig. 2 illustrates that this is not caused by poor quality of the simulation since all of the simulations of Re1 follow the theoretical hodograph quite closely and even overestimate the angle at the respective height by a little. In contrast to the higher **Re**, the veering of the wind vector continues in the lower parts of the boundary layer. Hence, for the low-**Re** case, the general observation of a higher $\alpha_\star$ with finer resolution is also caused by the approach of the final $\alpha_\star$ with decreasing height of

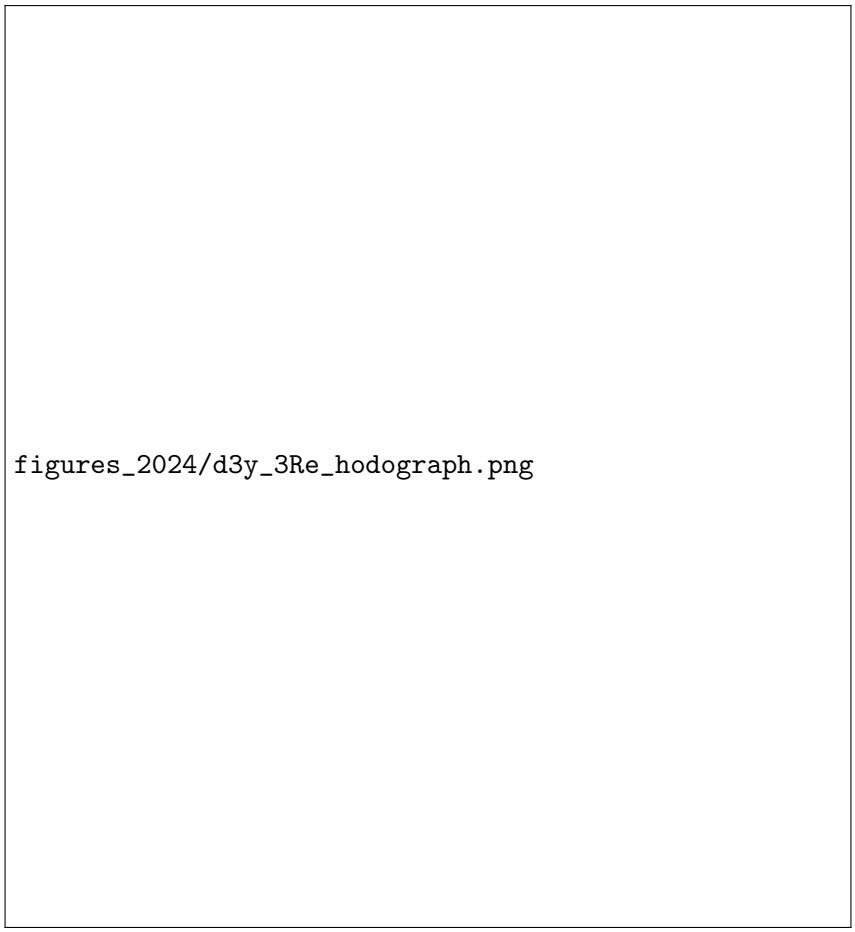

Figure 2: Geostrophy aligned hodographs of the LES in comparison to the theoretical and laminar hodographs. A $\times$ indicates the first grid point of the LES. At the points marked with $+$, the velocity is used to determine $u_\star$

the first grid point. In general, the finer resolved simulations show veering angles that are very close to the theoretical prediction.

4.2 Logarithmic layer stream-wise velocity

Figure 3 shows the velocity profiles from the LES and the theoretical profiles for each of the **Re**. In general, the velocity profiles of the LES agree well with the theoretical profiles: The course of the theoretical Ekman layer is matched and the simulations exhibit a logarithmic layer for the U-component. The lowest points of the LES of the higher **Re** fall into the logarithmic layer. For Re1, the lowest grid point falls into the buffer layer, which is visible as the curved course of the U-component below the logarithmic layer in the theoretical profile. The best resolved simulation with Deardorff-closure even seems to follow the course of the upper part of the buffer layer, but with a resolution of $\Delta^+ = 15$ this is a coincidence caused by a well-known S-shape of velocity profiles close to rigid walls Brasseur and Wei [2010]. This log-layer mismatch arises from a competition between the scales $u_\star$ and z and other velocity and length scales introduced by the discretization of the dynamical system [Mason and Thomson, 1992, Brasseur and Wei, 2010]. In other words, at the lower boundary, the relevant eddies are too small to be resolved by the grid and their contribution to the flow has to be modeled. Also the vertical component is massively restricted by the non-permeability of the wall, known as blocking effect. On the contrary, the SGS-closure assumes isotropic turbulence, which is not the case on the grid scale near the wall.

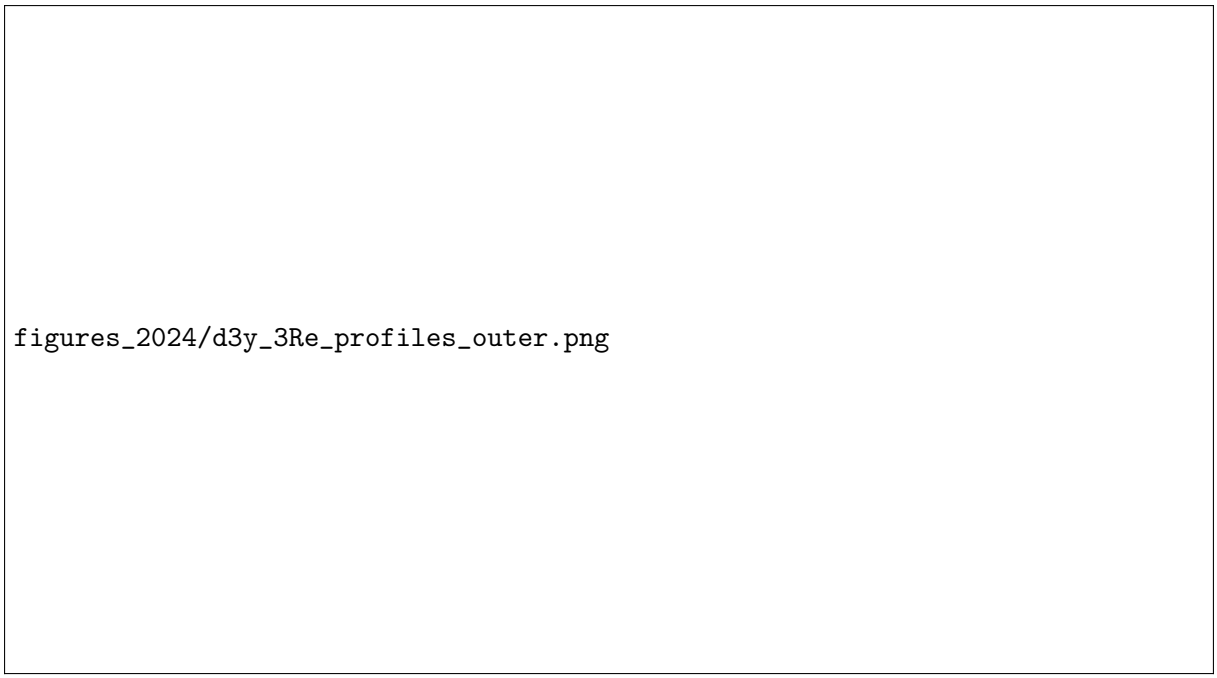

Figure 3: Shear-aligned velocity profiles in outer scaling. Solid lines: u-component, dashed lines: v-component. The lowest grid point is marked by x

In the logarithmic region, the profile of the u-component should follow the logarithmic law of eq. 4b with the Kármán measure $\kappa = (z^+ \partial U^+ / \partial z^+)^{-1} = const.$. In the low-Reynolds-number case, the viscous sublayer represents about 0.5% of the boundary layer, while this layer is not visible for the high-Reynolds-number cases, where the share drops to $10^{-5} - 10^{-7}$. Above the viscous sublayer, the theoretical profile shows a near-constant value for κ up to $z^- \approx 0.1$ for the case Re1 and up to $z^- \approx 0.12$ for the cases Re2 and Re3. In order to estimate κ_{LES} from the simulations, we perform a linear regression of the mean velocity in x-direction and the logarithm of height between the seventh grid point and the grid point corresponding to the height $z^- = 0.1$ for $Re1\_X$ and $z^- = 0.12$ for $Re2\_X$ and $Re3\_X$. We consider only points above the 7th grid point following arguments of Maronga et al. [2020b], that in PALM, the mean velocity profiles follow MOST above the seventh grid point. The number of values for each regression is 6, 12, and 18 for ReX_100, ReX_150 and ReX_200, respectively. We do not compute κ for ReX_50 since there are only six grid points below $z^- \approx 0.12$. The resulting κ_{LES} for the other simulations are shown in Tbl. 3. The coefficient of determination is above 0.99 for all fits. κ_{LES} is decreasing with finer resolution for all **Re**. While the values for ReX_100 are rather high with a value around 0.53, finer resolution leads to values closer to measurements around 0.46 for $Re1\_200$ and around 0.44 for $Re2\_200$ and $Re3\_200$. The dynamic subgrid closure yields lower values for κ_{LES}: in $Re1\_dyn$ we even see $\kappa_{LES} = 0.39$, while $Re2\_dyn$ and $Re3\_dyn$ yield 0.42 and 0.43, respectively. Figure 4 shows the Kármán measure in the logarithmic layer. For the simulations ReX_50, no constant κ can be observed. An increase in resolution leads to a profile of the Kármán measure closer to the theoretical curve for all cases. Close to the bottom, the Kármán measure is heavily influenced by the proximity of the wall and rather a function of the vertical index than of the physical distance from the wall. In accordance with the observations of Maronga [2014] and Maronga and Reuder [2017], the kinks in the Kármán measure diminish around the seventh grid point for all simulations. Above, the curve smoothens and approaches the expected value of κ (at least for the finer resolutions).

As expected for an LES with isotropic grid spacing, the resolution near the surface is a critical part of the simulation. We can support our above observations by taking a look at the two-point correlation in the critical layers of the simulations. The two point correlation is

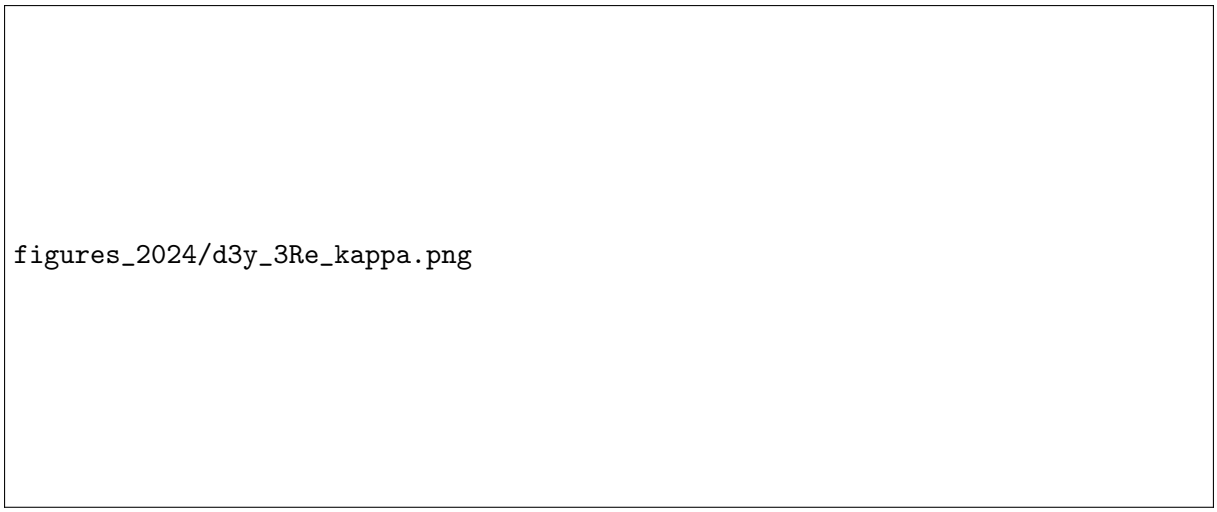

Figure 4: Kármán measure κ in the logarithmic region and above for different Reynolds numbers and resolutions

Figure 5: Two-point correlation of w-component in y-direction at $z^- \approx 0.08$. The horizontal line is at $B_{ww} = 0.3$

defined as

$$B_{xx}\left(x^*\right) = \langle u\left(x - x^*\right) u\left(x\right)\rangle / \sigma_u^2. \tag{16}$$

As suggested by Wurps et al. [2020], in an isotropic grid with periodic horizontal boundary conditions the turbulent structures of the velocity's w-component in y-direction can serve as an indicator how well the flow is resolved. Figure 5 shows the two-point correlation $B_{ww}(y^*)$ at a height of $z^- \approx 0.08$, which is right inside of the logarithmic layer. We define the average size of a structure in the flow σ as the distance where the two-point correlation drops to 0.3 (horizontal line in figure). The number of cells by which the average structure is resolved is equal to σ/Δ. All **Re** show a similar behaviour: the average size of the structure decreases with finer resolution and seems to approach a limit. The structure size of ReX_150 and ReX_200 are very close together, which indicates beginning convergence. Furthermore, the number of cells by which the structures are resolved exceed 4 from the resolution of ReX_150 on. This corresponds to the resolution from which on a logarithmic layer with a constant κ can be seen. It also fits to the rule of thumb given in Wurps et al. [2020], that in a sufficiently resolved part of an LES the average structures of the w-component in y-direction should be resolved by at least

4 cells. The dynamic closure shows structures that are slightly smaller than the structures of ReX_200, which is caused by a tendency to lower eddy-viscosities and, hence, a weaker coupling of neighboring grid cells.

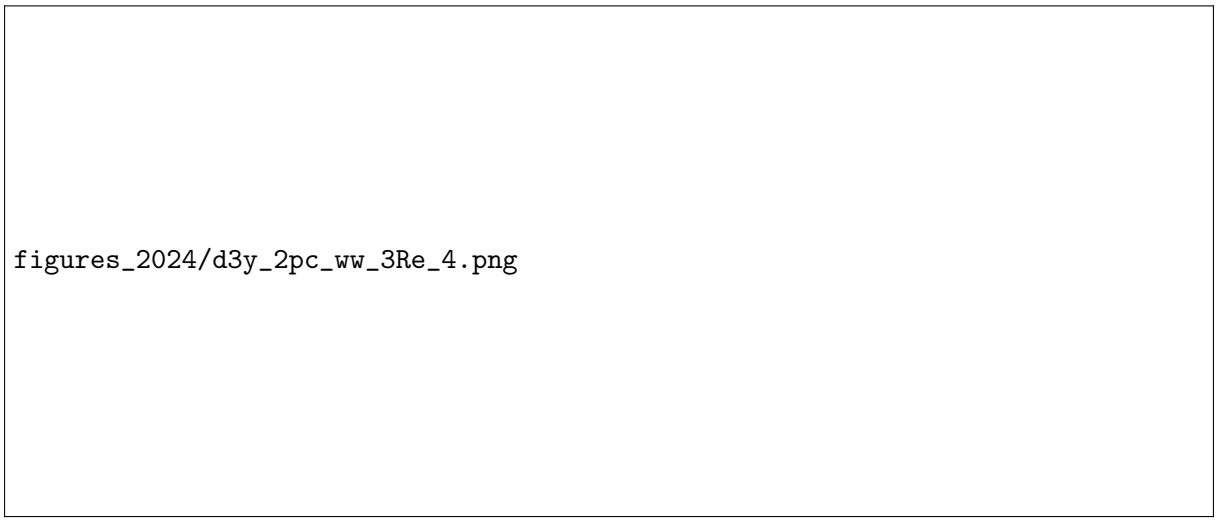

Figure 6: Two-point correlation of w-component in y-direction at the 8th grid point above the surface

Figure 6 shows $B_{ww}(y^*)$ at the 8th grid point above the bottom. Therefore, the corresponding heights differ between the simulations, that is $z^- = 0.16, 0.08, 0.053, 0.04, 0.04$ for ReX_50, ReX_100, ReX_150, ReX_200, ReX_dyn, respectively. For $Re1$, the curves almost collapse perfectly while for $Re2$ and $Re3$ we see slightly larger structures for ReX_50 and slightly smaller structures for ReX_dyn. This means that even 8 points above the lower boundary the smallest size of the turbulent structures rather depends on the grid cell size than on the actual height above the ground. According to the above findings and Maronga [2014], the flow should start to be well resolved from here on (above the seventh grid point). And indeed, the number of resolving cells is very close to 4 for $Re1$ and between 3 and 4 for $Re2$ and $Re3$, which is close to the recommended 4 cells.

4.3 Logarithmic layer span-wise velocity

Figure 7 shows the span-wise velocity component in the lower part of the boundary layer. [if we keep $V(z = \Delta)$ in the conclusion, add this here]. In the lowest part of $Re1$ ($z^- \lessapprox 0.05$), a part of the viscous layer is visible, where the velocity is slightly underestimated by the the LES. Above, the simulations $Re1\_200$ and $Re1\_dyn$ are very close to the theoretical curve. Lower resolution leads to an overestimation of the velocity in the logarithmic layer, which is consistent with a lack of large eddies that translates in a lack of mixing and thus a reduced turbulence level and increased velocity gradients. Around $z^- = 0.25$, while blending into the Ekman layer, the curves cross each other and the coarse simulations begin to underestimate the velocity. For the higher Re all simulations overestimate the velocity in the logarithmic layer, while coarser resolution leads to a higher velocity and finer resolution leads to a lower velocity and better agreement with the theoretical curve. Again, we see a crossing of the curves, between $z^- = 0.2$ and $z^- = 0.25$. A possible explanation of the fast increase and the steeper course of the coarser simulations is that the layers are coupled via less cells.

4.4 Ekman layer

Above the logarithmic layer, the Ekman layer follows, characterized by a change of wind direction. The course of the wind velocity vector is visualized by hodographs, as plotted in Fig. 2.

Figure 7: Span-wise velocity component in outer scaling

The hodograph of Re1_X is followed quite closely by all resolutions. Hence, all simulations of the low-**Re** case—even Re1_50—are resolved sufficiently to closely capture the course of the wind vector in the Ekman layer. The higher **Re** behave differently in the sense that the hodographs lie inside of the theoretical hodograph. An increased resolution ensures that at least the lowest grid point approaches the hodograph while the course of the hodograph's upper right part still does not reach the theoretical curve.

In Fig. 2, the cross indicates the lowest grid point and the plus indicates the height where the velocity for the boundary condition is taken from. To avoid taking a velocity from the first layer of the simulation, where the turbulent flow is poorly resolved, we took the horizontal velocity near $z^- = 0.1$, where the mean velocity already veered away from the direction of the surface stress by around one third of α. However, the veering does not seem to influence the resulting bulk stress $u_\star$ at the bottom: all but the coarsest resolutions yield a $u_\star$ very close to the theoretic reference.

Figure 8 shows the shear-aligned velocity deficit $U^- - U_G^-$ (v-component accordingly) of the whole boundary layer. The strongest deviations from the theoretical profiles can be seen for the coarsest LES near the super-geostrophic maximum of the U-component. Finer resolution leads to a very good agreement with the extent of the maximum, which also holds for the higher **Re**. The super-geostrophic maximum is a consequence of vertical redistribution of momentum across the ABL; less redistribution leads to a less pronounced maximum. At the same time, of course, one would expect an increased level of turbulence to cause a flatter hodograph. BUT, the surface veering is set rather by the interplay of MOST and the prescribed roughness while the profile in the Ekman layer is a resolved quantity. However, for higher Reynolds numbers $Re2$ and $Re3$, the maximum velocity in x-direction is still not reached by the LES and the approach of the geostrophic wind in the upper part of the boundary layer takes place at lower heights than in theory. This is even more obvious for the V-component, where the maximum value is at a significantly lower height than in the theoretical curve. In general, a finer resolution leads to a lower location of the maximum. The maximum at lower heights might also explain the too high velocities in the logarithmic layer for the higher Re.

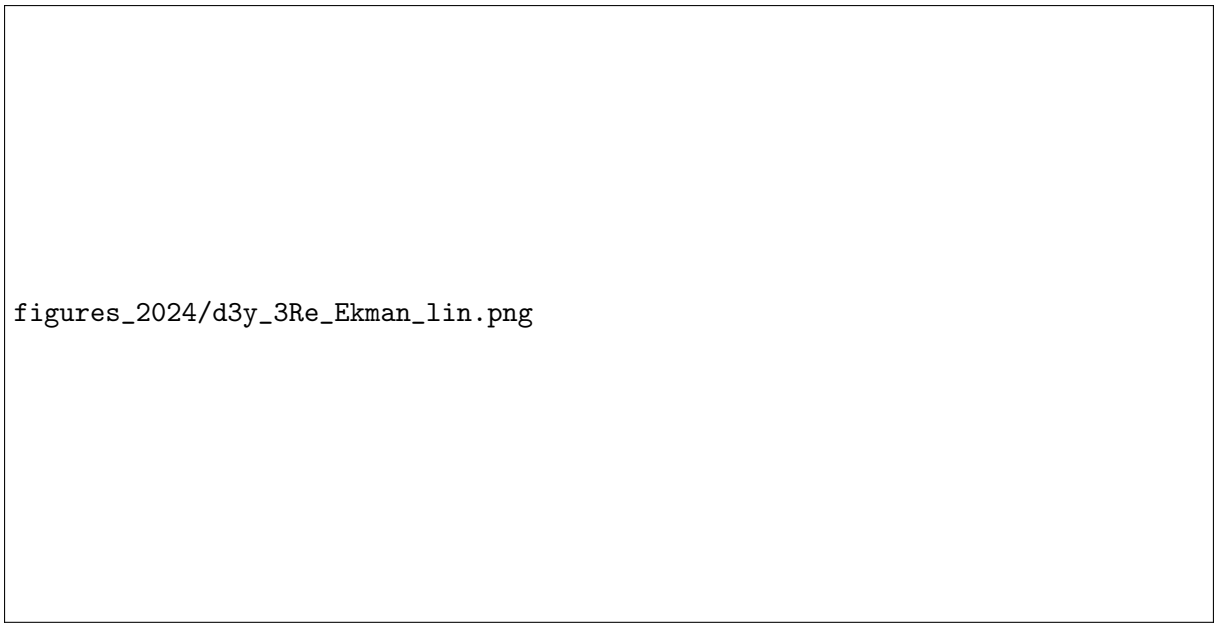

Figure 8: Shear-aligned velocity deficit in outer scaling. Solid lines: U-component, dashed lines: V-component

5 Conclusions

We studied truly neutral Ekman boundary layers—absent of capping inversions, non-stationarity, and surface heterogeneity. For the first time, an LES of the Ekman layer is *a posteriori* validated against a DNS for an identical configuration. Despite the common assumption that viscosity as a parameter drops out in LES as a consequence of the turbulence closure, we considered a range of scale separations (Reynolds numbers) and found that for an exact representation of the surface turning and wall friction as well as the wind-turning profile, viscous effects need consideration. We derive an analytical relation demonstrating that — given fixed surface properties — the specification of z_0 implicitly defines a viscosity. The LES suffer from the dilemma, that in Ekman flow, some aspects of crucial importance happen on relatively small scales, such as the rotation-surface interaction which is confined to the inner layer.

With the wind-profile formulation developed in Part 1 of this work, we have a reference based on first principles for intermediate-Re simulations, and a quasi-reference for the higher-Re simulations. While we acknowledge that both the LES and the wind-profile model suffer from assumptions for high Reynolds number, their quantitative agreement across a wide range of scale separations hints towards the consistency. In particular, we understand that the grid convergence of LES towards the theoretical profiles underpins the inviscid scaling hypotheses in the development of the theory underlying part 1 of this paper.

We simulated three different Reynolds numbers while having DNS results for the lowest **Re**. For the low **Re**, viscous forces have a significant contribution to the balance of forces on the grid scale of the LES, hence we adapted the LES code to consider the fluid's viscosity in addition to the modeled eddy-viscosity. We did not introduce a roughness length z_0 at the lower boundary as additional parameter but deduced z_0 according to the law of the wall and the shear velocity expected according to the semi-empirical law by Spalart [1989]. The interplay of geostrophic wind, shear velocity, and roughness length in the simulation showed remarkable consistency, which supports the value of the adapted boundary condition at the bottom [Maronga and Reuder, 2017]. The dependence of the LES solution on the grid cell size was investigated through a comparison of four different resolutions. The setups of all **Re** use similar grid sizes in terms of the outer scale ($\Delta^- = \Delta/\delta = const.$) but different grid sizes in terms of the inner

scale ($\Delta^+ = \delta^+ \cdot const. = Re_\tau \cdot const.$). This means that from an inner scale perspective the high Reynolds numbers were much less well resolved.

The convergence towards the theoretical profile expressed itself in different major aspects of the flow. To reach the expected total rotation $\alpha_\star$, a sufficient resolution was necessary. Furthermore, a sufficient vertical resolution was needed to simulate a logarithmic layer with a constant Kármán measure in some vertical extent.

A resolution of 150 grid levels below δ resolves well the boundary layer across all **Re**, in agreement with the findings of Wurps et al. [2020]. Their study demonstrated successful resolution of the neutral simulation with more than 100 grid levels within the boundary layer δ_{95}. The ratio δ_{95}/δ is approximately 2/3 (gradually decreasing with Reynolds number). Therefore, having 150 grid levels within δ roughly corresponds to around 100 grid levels within δ_{95}.

In summary, we synthesize some technical recommendations for the correct simulation of Ekman layer dynamics on a process level:

- The roughness parameter (z_0) essentially defines a Reynolds number of the LES Problem
- $V|_{z=\Delta} < u_\star$ for an accurate matching of the hodograph and proper quantification of $\alpha_\star$. [where is this in the results?]
- There should exist a logarithmic layer, or explicit consideration of viscous interaction with the surface; otherwise the assumptions of the surface closure (MOST / dynamic wall model) will fail.
- The parameters $\alpha_\star$ and $u_\star$ characterizing the bulk Ekman dynamics (across the vertical extent of the boundary layer) are matched by the LES if—in a three-dimensionally isotropic grid—more than 150 grid points are used in the vertical direction.
- For very high resolution or relatively small Reynolds number, the viscous friction needs to be taken into account as the modeled eddy viscosity may locally drop to zero.

When these considerations are taken into account, LES becomes possible at uncommonly low Reynolds number and resolution, which allows a quantitative comparison to state-of-the art DNS.

Some resolution and best-practice constraints developed in this work are strong, in some cases even prohibitive. They result from the externality of the flow, i.e. the presence of non-turbulent fluid aloft which leads to a duality of scales (cf. section 2): both the inner and outer dynamics need to be visible to the resolved LES scales, at least to some extent. Despite these relatively strong constraints, we appreciate the capability of LES which, for example in case Re3, can appropriately match both $u_\star$, $\alpha_\star$ and the hodograph with the first grid point located at about 10^6 wall units. This means, there is a gap in resolution in comparison to a true DNS of five to six orders of magnitude per direction; illustrating that a DNS at this scale would be prohibitive and will remain so for a foreseeable time. From this inner, or small-scale perspective, a requirement of few hundred grid points across the boundary layers is not a lot.

We did not see a second logarithmic layer as Jiang et al. [2018] neither in the theoretical formulation nor in our simulations. A reason might be their introduction of the additional parameter z_0. [keep this paragraph? After our discussion about the change of Re when introducing a roughness length I don't believe this explanation anymore...]

The theoretical formulation of mean velocity profiles within the turbulent Ekman layer can serve as benchmark for model frameworks such as LES. These reference profiles offer a deeper analysis beyond the conventional assessment of the logarithmic increase in wind speed within the Prandtl layer. Comparing simulation results to the expected bulk parameters $u_\star$ and $\alpha_\star$ and to the hodograph and conducting a detailed evaluation of the wind speed profiles can yield valuable insights into the correct interplay among the model's grid resolution, turbulence closure, and boundary conditions. In the future, expanding the theoretical profiles to include additional

aspects, such as temperature stratification, could potentially provide an even more valuable reference.

6 Acknowledgements

The simulations were performed at the HPC Cluster EDDY, located at the University of Oldenburg (Germany) and funded by the Federal Ministry for Economic Affairs and Energy (Bundesministeriums für Wirtschaft und Energie) under grant number 0324005.

References

Cedrick Ansorge and Juan Pedro Mellado. Global intermittency and collapsing turbulence in the stratified planetary boundary layer. *Boundary-Layer Meteorology*, 153(1):89–116, 2014.

Roni Avissar and R A Pielke. A Parameterization of Heterogeneous Land Surfaces for Atmospheric Numerical-Models and Its Impact on Regional Meteorology. *Monthly Weather Review*, 117(10):2113–2136, October 1989. doi: 10.1175/1520-0493(1989)117¡2113:APOHLS¿2.0.CO;2.

James G Brasseur and Tie Wei. Designing large-eddy simulation of the turbulent boundary layer to capture law-of-the-wall scaling. *Phys Fluids*, 22(2):021303, 2010.

S-P Breton, J Sumner, Jens Nørkær Sørensen, Kurt Schaldemose Hansen, Sasan Sarmast, and Stefan Ivanell. A survey of modelling methods for high-fidelity wind farm simulations using large eddy simulation. *Philosophical Transactions of the Royal Society A: Mathematical, Physical and Engineering Sciences*, 375(2091):20160097, 2017.

Wilfried Brutsaert. A theory for local evaporation (or heat transfer) from rough and smooth surfaces at ground level. *Water Resources Research*, 11(4):543–550, 1975. ISSN 1944-7973. doi: 10.1029/WR011i004p00543.

Martin Claussen. Estimation of areally-averaged surface fluxes. *Boundary-Layer Meteorol*, 54 (4):387–410, March 1991. ISSN 0006-8314, 1573-1472. doi: 10.1007/BF00118868.

GT Csanady. On the "resistance law" of a turbulent ekman layer. *Journal of Atmospheric Sciences*, 24(5):467–471, 1967.

James W Deardorff. Stratocumulus-capped mixed layers derived from a three-dimensional model. *Boundary-Layer Meteorology*, 18(4):495–527, 1980.

Vagn Walfrid Ekman. On the influence of the earth's rotation on ocean currents. *Ark. Mat. Astron. Fys., Vol. 2 (1905), pp. 1-53*, 2:1–53, 1905.

I Esau. Simulation of ekman boundary layers by large eddy model with dynamic mixed subfilter closure. *Environmental Fluid Mechanics*, 4(3):273–303, 2004.

Evgeni Fedorovich, Robert Conzemius, and Dmitrii Mironov. Convective entrainment into a shear-free, linearly stratified atmosphere: Bulk models reevaluated through large eddy simulations. *Journal of the atmospheric sciences*, 61(3):281–295, 2004.

C García-Sánchez, J van Beeck, and C Gorlé. Predictive large eddy simulations for urban flows: Challenges and opportunities. *Building and Environment*, 139:146–156, 2018.

J. R. Garratt. The internal boundary layer ? A review. *Boundary-Layer Meteorol*, 50(1-4): 171–203, March 1990. ISSN 0006-8314, 1573-1472. doi: 10.1007/BF00120524.

Filippo Giorgi and Roni Avissar. Representation of heterogeneity effects in Earth system modeling: Experience from land surface modeling. *Rev. Geophys.*, 35(4):413–437, November 1997. ISSN 87551209. doi: 10.1029/97RG01754.

Beom-Soon Han, Jong-Jin Baik, Kyung-Hwan Kwak, and Seung-Bu Park. Large-eddy simulation of reactive pollutant exchange at the top of a street canyon. *Atmospheric Environment*, 187: 381–389, 2018.

Stefan Heinz. Realizability of dynamic subgrid-scale stress models via stochastic analysis. *Monte Carlo Methods Appl*, 14(4):311–329, 2008.

Qingfang Jiang, Shouping Wang, and Peter Sullivan. Large-eddy simulation study of log laws in a neutral ekman boundary layer. *Journal of the Atmospheric Sciences*, 75(6):1873–1889, 2018.

Soshi Kawai and Johan Larsson. Wall-modeling in large eddy simulation: Length scales, grid resolution, and accuracy. *Physics of fluids*, 24(1), 2012.

Andrey Nikolaevich Kolmogorov. Dissipation of energy in the locally isotropic turbulence. In *Dokl. Akad. Nauk SSSR A*, volume 32, pages 16–18, 1941.

Jonathan A Kostelecky and Cedrick Ansorge. Simulation and scaling analysis of periodic surfaces with small-scale roughness in turbulent Ekman flow. *J Fluid Mech*, 2024. doi: 10.1017/jfm.2024.542.

Helmut Kraus. *Grundlagen der Grenzschicht-Meteorologie: Einführung in die Physik der atmosphärischen Grenzschicht und in die Mikrometeorologie*. Springer, 2008.

Douglas K Lilly. On the instability of ekman boundary flow. *Journal of Atmospheric Sciences*, 23(5):481–494, 1966.

Björn Maronga. Monin–obukhov similarity functions for the structure parameters of temperature and humidity in the unstable surface layer: Results from high-resolution large-eddy simulations. *Journal of the Atmospheric Sciences*, 71(2):716–733, 2014.

Björn Maronga and Joachim Reuder. On the formulation and universality of monin–obukhov similarity functions for mean gradients and standard deviations in the unstable surface layer: Results from surface-layer-resolving large-eddy simulations. *Journal of the Atmospheric Sciences*, 74(4):989–1010, 2017.

Björn Maronga, Sabine Banzhaf, Cornelia Burmeister, Thomas Esch, Renate Forkel, Dominik Fröhlich, Vladimir Fuka, Katrin Frieda Gehrke, Jan Geletič, Sebastian Giersch, et al. Overview of the palm model system 6.0. *Geoscientific Model Development*, 13(3):1335–1372, 2020a.

Björn Maronga, Christoph Knigge, and Siegfried Raasch. An improved surface boundary condition for large-eddy simulations based on monin–obukhov similarity theory: evaluation and consequences for grid convergence in neutral and stable conditions. *Boundary-Layer Meteorology*, 174(2):297–325, 2020b.

Paul J Mason and David J Thomson. Stochastic backscatter in large-eddy simulations of boundary layers. *Journal of Fluid Mechanics*, 242:51–78, 1992.

D Mehta, AH Van Zuijlen, B Koren, JG Holierhoek, and H Bijl. Large eddy simulation of wind farm aerodynamics: A review. *Journal of Wind Engineering and Industrial Aerodynamics*, 133:1–17, 2014.

A S Monin. The Atmospheric Boundary Layer. *Annual Review of Fluid Mechanics*, 2:225–250, 1970. doi: 10.1146/annurev.fl.02.010170.001301.

Wim Munters, Charles Meneveau, and Johan Meyers. Shifted periodic boundary conditions for simulations of wall-bounded turbulent flows. *Physics of Fluids*, 28(2), 2016.

AM Obukhov. On the distribution of energy in the spectrum of turbulent flow. *Bull. Acad. Sci. USSR, Geog. Geophys.*, 5:453–466, 1941.

Michael Optis, Adam Monahan, and Fred C Bosveld. Moving beyond monin–obukhov similarity theory in modelling wind-speed profiles in the lower atmospheric boundary layer under stable stratification. *Boundary-layer meteorology*, 153(3):497–514, 2014.

Stephen B Pope. Ten questions concerning the large-eddy simulation of turbulent flows. *New J Phys*, 6(1):35, 2004.

Fernando Porté-Agel, Yu-Ting Wu, Hao Lu, and Robert J Conzemius. Large-eddy simulation of atmospheric boundary layer flow through wind turbines and wind farms. *J Wind Eng Ind Aerodyn*, 99(4):154–168, 2011.

M. R. Raupach, R. A. Antonia, and S. Rajagopalan. Rough-Wall Turbulent Boundary Layers. *Applied Mechanics Reviews*, 44(1):1–25, January 1991. ISSN 0003-6900. doi: 10.1115/1.3119492.

Philippe R Spalart. Theoretical and numerical study of a three-dimensional turbulent boundary layer. *Journal of Fluid Mechanics*, 205:319–340, 1989.

Philippe R Spalart, Gary N Coleman, and Roderick Johnstone. Direct numerical simulation of the ekman layer: A step in reynolds number, and cautious support for a log law with a shifted origin. *Physics of Fluids*, 20(10):101507, 2008.

Rob Stoll, Jeremy A Gibbs, Scott T Salesky, William Anderson, and Marc Calaf. Large-eddy simulation of the atmospheric boundary layer. *Boundary-Layer Meteorology*, 177:541–581, 2020.

Roland B. Stull. *An Introduction to Boundary Layer Meteorology*. Atmospheric Sciences Library. Kluwer Academic Publishers, Dordrecht ; Boston, 1988. ISBN 978-90-277-2768-8 978-90-277-2769-5.

H Tennekes. The logarithmic wind profile. *Journal of the Atmospheric Sciences*, 30(2):234–238, 1973.

Hauke Wurps, Gerald Steinfeld, and Stefan Heinz. Grid-resolution requirements for large-eddy simulations of the atmospheric boundary layer. *Boundary-Layer Meteorology*, 175(2):179–201, 2020.